JOURNAL OF GEOPHYSICAL RESEARCH, VOL. 106, NO. D22, PAGES 28,243-28,258, NOVEMBER 27, 2001

Microwave polarized signatures generated within cloud systems: Special Sensor Microwave Imager (SSM/I) observations interpreted with radiative transfer simulations

Catherine Prigent[1] and Juan R. Pardo[2]
Columbia University, NASA Goddard Institute for Space Studies, New York, USA

Michael I. Mishchenko and William B. Rossow
NASA Goddard Institute for Space Studies, New York, USA

Abstract. Special Sensor Microwave Imager (SSM/I) observations in cloud systems are studied over the tropics. Over optically thick cloud systems, the presence of polarized signatures at 37 and 85 GHz is evidenced and analyzed with the help of cloud top temperature and optical thickness extracted from visible and IR satellite observations. Scattering signatures at 85 GHz (TbV(85)$\leq$250 K) are associated with polarization differences $\geq$ 6 K ~50% of the time over ocean and ~40% over land. In addition, over thick clouds the polarization difference at 37 GHz rarely is negligible. The polarization differences at 37 and 85 GHz do not stem from the surface but are generated in regions of relatively homogeneous clouds having high liquid water content. To interpret the observations, a radiative transfer model that includes the scattering by nonspherical particles is developed, based on the T matrix approach and using the doubling and adding method. In addition to handling randomly and perfectly oriented particles this model can also simulate the effect of partial orientation of the hydrometeors. Microwave brightness temperatures are simulated at SSM/I frequencies and are compared with the observations. Polarization differences of $\sim$ 2 K can be simulated at 37 GHz over a rain layer, even using spherical drops. The polarization difference is larger for oriented nonspherical particles. The 85 GHz simulations are very sensitive to the ice phase of the cloud. Simulations with spherical particles or with randomly oriented nonspherical ice particles cannot replicate the observed polarization differences. However, with partially oriented nonspherical particles the observed polarized signatures at 85 GHz are explained, and the sensitivity of the scattering characteristics to the particle size, asphericity, and orientation is analyzed. Implications on rain and ice retrievals are discussed.

1. Introduction

Passive microwave satellite observations have been extensively studied to estimate cloud properties and precipitation on a global scale. Depending on the observed wavelength and on the cloud and rain characteristics, the microwave radiation is affected by emission, absorption, and scattering within the hydrometeor layers. During the emission/absorption process, liquid particles cause brightness temperatures to increase over a radiatively cold background like the ocean; the induced warming of the signal increases with frequency up to a saturation level. Retrievals of cloud liquid water paths over ocean are currently based on the emission signals measured between 19 and 85 GHz [e.g., *Greenwald et al.*, 1993; *Liu and Curry*, 1993; *Phalippou*, 1996; *Lin and Rossow*, 1994; *Prigent et al.*, 1997; *Wentz*, 1997]. Emission-based algorithms have also been developed to estimate precipitation [*Wilheit et al.*, 1977; *Prabhakara et al.*, 1992]. In contrast, scattering by large hydrometeors (particle dimensions $\geq$200 μm) reduces the amount of radiation measured by the satellite, es-

---

[1] Now at Centre National de la Recherhe Scientifique, Département de Radioastronomie Millimétrique, Observatoire de Paris, Paris, France.

[2] Now at Consejo Superior de Investigaciones Cientificas, Instituto de la Estructura de la Materia, Departemento de Fisica Molecular, Madrid, Spain.

Paper number 2001JD900242.
0148-0227/01/2001JD900242$09.00

pecially at higher frequencies. The scattering signal at 85.5 GHz has been used, for example, by *Spencer et al.* [1989], *Grody* [1991], *Ferraro et al.* [1996], and *Mohr et al.* [1999] to estimate precipitation over ocean and land. The emission signal originates in the liquid lower part of the cloud and rain, whereas the scattering in the upper part of the cloud modulates the emission signal, especially at high frequencies. For each frequency the radiation measured by the satellite radiometer is determined by the vertical structure of the hydrometeors, with their specific phase, size distribution, and shape. Modeling of the microwave radiative transfer in precipitating cloud systems, including emission and scattering processes, has been used to derive precipitation retrieval algorithms [e.g., *Smith et al.*, 1992; *Mugnai et al.*, 1993; *Kummerow and Giglio*, 1994]. On the basis of elaborate cloud microphysics obtained from cloud resolving models, radiative transfer calculations are performed for detailed hydrometeor profiles taking into account different hydrometeor phases and various size distributions that depend on the life stage of the cloud structure. The scattering properties of the particles are calculated from Mie theory assuming spherical hydrometeors. Although the emission from the Earth's surface can be polarized, these studies usually do not account for generation of polarization within the hydrometeor layers. To further understand the microwave signatures in cloud and precipitation, high-resolution passive microwave observations have been performed from high-altitude aircraft [e.g., *Adler et al.*, 1990; *Fulton and Heymsfield*, 1991; *Turk et al.*, 1994; *MacGaughey et al.*, 1996], but because of the large resolution differences the extrapolation to satellite observations is difficult [*MacGaughey et al.*, 1996]. *Panegrossi et al.* [1998] recently stressed the need for consistency between models and measurements for precipitation retrievals based on elaborate cloud microphysics. The cloud model and the associated radiative transfer model have to be able to explain and reproduce all the observed signatures.

Although the microwave radiative properties of clouds and rain have been widely explored from model simulations to observations from satellites and aircrafts, some features of the measured microwaves are still not fully explored. Polarized scattering signatures have already been observed in some cloud structures, both from satellite and aircraft measurements. *Spencer et al.* [1983] observed residual polarization at 37 GHz with the Scanning Multichannel Microwave Radiometer (SMMR) in precipitation areas but later attributed it to calibration problems [*Spencer et al.*, 1989]. However, *Spencer et al.* [1989, p.265] did observe polarization differences at 85 GHz with the Special Sensor Microwave Imager (SSM/I) and attributed this difference to nonspherical particles with non-random orientations in stratiform regions, whereas in convective cores the absence of polarization would be due to "irregularly shaped graupels tumbling in a turbulent environment". *Heymsfield and Fulton* [1994] also observed polarized scattering signatures at 85 GHz with SSM/I (up to 13 K difference between the vertical and horizontal brightness temperatures) in a few mesoscale systems over land and ocean. They also believe these are related to large nonspherical ice particles with a preferred horizontal orientation in the stratiform region of the mesoscale cloud, but they did no radiative transfer simulations to support their assumption. With the ER-2 aircraft over land, *Adler et al.* [1990] observed residual polarizations of several kelvins at 37 and 18 GHz in convective areas. Very recently, *Petty* [2001] performed a principal component analysis of the SSM/I radiances to help characterize the scattering signatures in tropical stratiform rainfall.

Haferman [1999] thoroughly reviews the studies on the effect of nonspherical hydrometeors on microwave radiation. The various model studies show that oriented nonspherical hydrometeors are necessary to generate large polarized scattering signatures in the microwave domain. *Wu and Weinman* [1984] obtain small polarization differences at 37 GHz (~1 K) with spherical particles, whereas incorporating nonspherical particles in the calculation could yield ~10 K for the same frequency for large rain rate ($\geq$ 32 mm/h). *Evans and Vivekanandan* [1990] concentrate on the radiative properties of horizontally oriented cirrus crystals (plates, columns, and needles) at 37, 85, and 157 GHz. *Turk and Vivekanandan* [1995] consider ice plates, oblate raindrops, and conical graupels and calculate large polarization differences at 37 and 85 GHz. *Czekala and Simmer* [1998] analyze the polarization difference generated by horizontally oriented spheroidal liquid particles on upward and downward brightness temperatures. Large polarization differences are simulated and are confirmed by ground-based observations at 37 GHz [*Czekala et al.*, 2001]. *Roberti and Kummerow* [1999] use a Monte Carlo code to simulate the effect of horizontally oriented nonspherical particles at 37 and 85 GHz. Using cloud profiles from atmospheric mesoscale model, they reproduce the observations by *Heymsfield and Fulton* [1994] when tuning the amount of nonspherical particles. However, the same matrices are used for horizontally oriented and randomly oriented particles, whereas angle-dependent matrices should be calculated for oriented particles.

In this study, SSM/I microwave observations in cloud systems are analyzed over the tropics for several months, along with the International Satellite Cloud and Climatology Project (ISCCP) infrared and visible derived cloud products which include cloud top temperature and optical thickness (section 2). The presence of strongly polarized scattering signatures at 85 GHz is examined with the help of lower-frequency microwave measurements and ISCCP parameters: Their frequency of occurrence and their characteristics are statistically analyzed over land and ocean separately. At 37 GHz, residual polarization difference is observed, even over optically thick hydrometeor layers. A radiative transfer model that includes emission/scattering by nonspherical particles is developed, based on the T matrix approach [*Mishchenko et al.*, 1991, 1993, 1999] and the formalism of gas absorption by *Pardo et al.* [2001a, 2001b]. The radiative transfer is carried out using the doubling and adding method as described by *Evans and Stephens* [1995]. The code not only treats randomly or perfectly oriented particles, it can also simulate partially oriented spheroidal particles. With plausible hydrometeor profiles the microwave observations are reproduced and the scattering signatures are explained (section 3). Section 4 concludes this study and stresses the importance of a good understanding of the emission/scattering mechanisms when developing rain and ice retrievals.

2. SSM/I Observations of Polarized Scattering Signatures Generated by Clouds

2.1. Satellite Data

The Defense Meteorological Satellite Program (DMSP) satellites provide an almost complete coverage of the Earth twice daily from near-polar, circular, Sun-synchronous orbits. The SSM/I instrument on board these satellites senses the atmospheric and surface emissions at 19.35, 22.235, 37.0, and 85.5 GHz with both horizontal and vertical polarizations, except the 22 GHz frequency, which has vertical polarization only [*Hollinger et al.*, 1987]. The observing incident angle on the Earth is close to 53°, and the elliptical fields of view (the footprint at -3 dB) decrease in size proportionally with frequency, from 43×69, 40×50, and 28×37 to 13×15 km for 19.35, 22.235, 37.0, and 85.5 GHz, respectively. An instrument evaluation has been performed by *Hollinger et al.* [1990], and an intersensor calibration has recently been completed by *Colton and Poe* [1999]. Results from the F10 and F11 satellites are presented.

In the ISCCP data, cloud parameters and related quantities are retrieved from visible (VIS, $\sim$0.6 μm wavelength) and infrared (IR, $\sim$11 μm wavelength) radiances provided by a set of polar and geostationary meteorological satellites [*Rossow and Schiffer*, 1991, 1999]. Among other variables, the ISCCP data set provides cloud top temperatures. During daytime, when visible reflectances are available, the cloud optical thickness in the VIS is also retrieved, assuming a cloud drop size distribution. For liquid water clouds (i.e., for clouds with cloud top temperatures above 260 K) an effective radius of 10 μm is assumed to estimate the cloud liquid water path, whereas for ice clouds (i.e., cloud top temperatures below 260 K) the effective radius of polycrystals is assumed to be 30 μm to retrieve the ice path. The pixel level data set (the DX data set) is used. A detailed description of the ISCCP data products is provided by *Rossow et al.* [1996]. The ISCCP DX horizontal sampling of $\sim$30 km is fully compatible with the SSM/I observations that are sampled at 25 km. ISCCP DX images are available every 3 hours and for each SSM/I pixel, the closest in time is selected, meaning that the ISCCP DX and SSM/I observations are coincident to within ±1.5 hours. As will be discussed later in section 2.2, the signatures of interest in this study are mostly observed in stratiform clouds where the time difference between the observations does not much affect the statistical analysis that is performed.

2.2. Polarized Scattering Signatures over Optically Thick Clouds

An analysis of SSM/I observations along with collocated ISCCP data is first conducted. Because polarized scattering signatures over clouds do not occur frequently, a statistical analysis is better suited to understand their dominant features. Three months (July 1992, October 1992, and January 1993) have been examined. Only observations over tropical areas are presented here. Midlatitude and polar regions have also been studied but are not shown in this paper: Polarized signatures from clouds are less frequent and much weaker in these areas, and confusions can arise from scattering and reflection by snow and ice surfaces. Two specific situations are considered in the tropics, one over ocean and the other over land.

For July 1992 and the latitudinal band from 30°S to 30°N, Plate 1 presents scatterplots of the SSM/I brightness temperatures in the vertical polarization (TbV) versus the brightness temperature polarization differences (TbV-TbH). This is done for three SSM/I frequencies (19, 37, and 85 GHz) and for cloudy pixels only (cloudiness is determined by the ISCCP pixel closest in time and space). The sea and land cases are treated separately. For each 1×1 K box, the color indicates the mean cloud top temperature as given by ISCCP. Contours limit regions where the pixel population in the 1×1 K boxes is larger than 0.01% and 0.002% of the total population for a month. In Plate 1 the emission and scattering regimes are easily recognizable over ocean. The two lower frequencies respond primarily to emission/absorption processes. In the emission regime over the ocean cold background, thinner clouds show rather low microwave brightness temperatures with large polarization differences caused by the ocean surface. As cloud opacity increases, usually associated with a decrease of the cloud top temperature, the microwave brightness temperatures increase and the polarization differences progressively decrease. In the scattering regime, which is only clearly observable at 85 GHz for clouds with cold top temperatures, the brightness temperatures decrease due to scattering by larger cloud particles. Scattering signatures at 37 GHz are not obvious, although for low cloud top temperature, TbV(37) decreases with nonzero polarization differences. Over land, large differences in surface emissivities (from low emissivities over wet soil to emissivity $\sim$1 over dense vegetation) make the interpretation of the scatterplots more difficult. The polarization difference produced by the land surface is generally limited, except over desert and inundated surfaces. However,

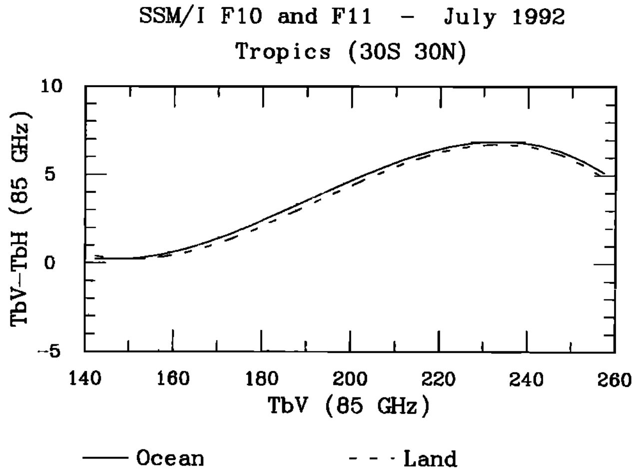

Figure 1. Statistically most probable polarization difference at 85 GHz versus the 85 GHz vertically polarized brightness temperature over ocean and land.

the cloud scattering signal at 85 GHz is still easily recognized, associated with high opacity clouds that are likely to block any signal from the surface. The relative population of pixels for TbV(85) $\leq$ 220 K is larger over land than over ocean (see the population contours in Plate 1).

At 85 GHz where scattering dominates the signal, the polarization difference is clearly greater than zero. In the scattering regime, Figure 1 presents the statistically most probable polarization difference versus the vertically polarized brightness temperature, both observed at 85 GHz over ocean and land. With decreasing TbV(85), the mean polarization difference first increases up to ~7 K for TbV~ 230 K and decreases down to zero. For 200 K$\leq$ TbV(85)$\leq$ 260 K the most probable polarization difference is $\geq$ 5 K, both over ocean and land. In regions of thick clouds (cloud top temperatures below 230 K), scattering signatures (TbV(85)$\leq$250 K) are associated with polarization differences $\geq$ 6 K for ~50% of the time over ocean and for ~40% over land.

To better characterize the scattering signatures at 85 GHz, Figure 2 focuses on the scattering regime at 85 GHz and presents histograms of the ISCCP cloud top temperatures for each 10 K TbV and 3 K (TbV-TbH) interval at 85 GHz for July 1992 over the tropics. Ocean (solid lines) and land (dashed lines) cases are treated separately. Histograms are only presented when the number of pixels falling in the interval is larger than 70 during the month. While TbV(85) changes drastically from 240 to 140 K, the corresponding cloud top temperatures do not undergo significant changes, with mode values around 210 K when 85 GHz falls below 240 K, both over ocean and land, decreasing to ~200 K when TbV(85) gets below 190 K. The IR radiation is less sensitive to the mechanisms that induce large differences in the 85 GHz brightness temperature and

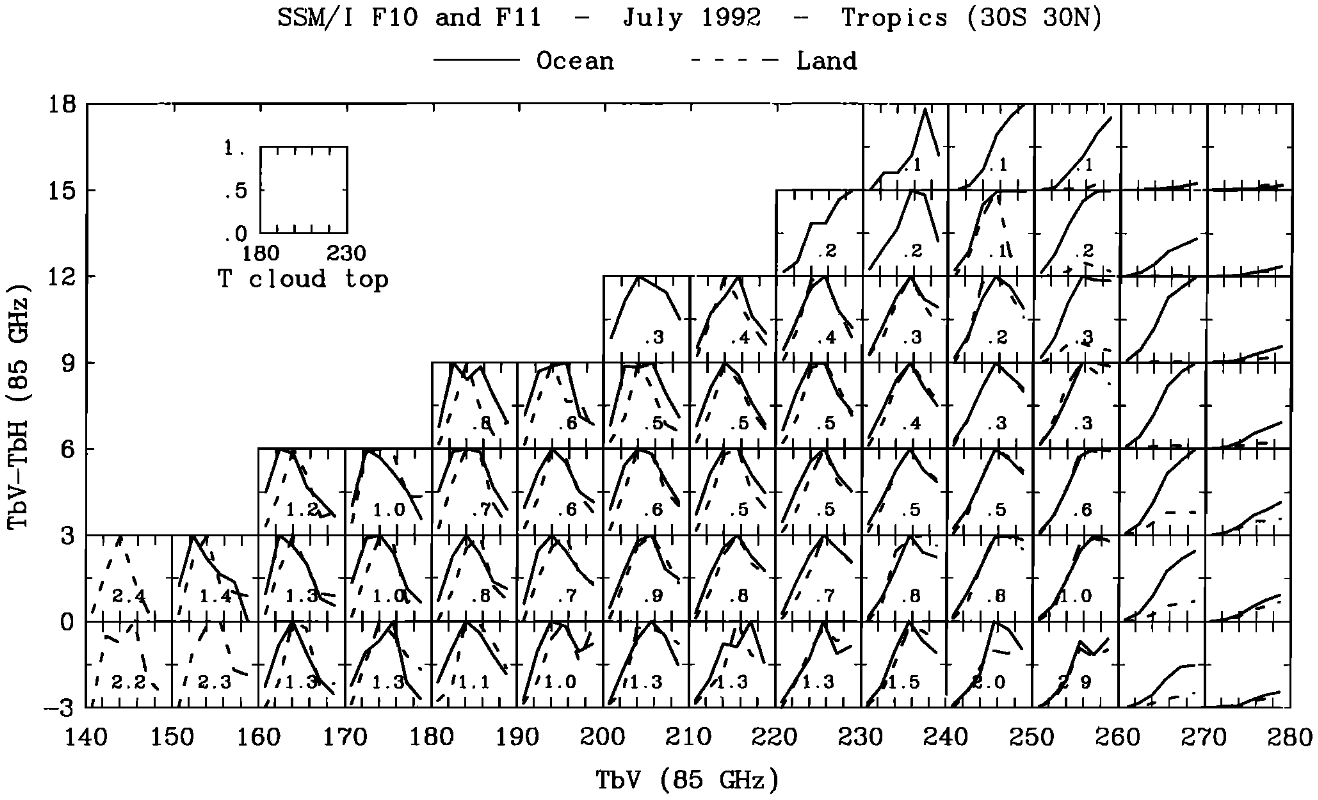

Figure 2. Histograms of the ISCCP cloud top temperatures for each 10 K TbV and 3 K TbV-TbH box at 85 GHz for July 1992 over the tropics. Ocean (solid lines) and land (dashed lines) cases are treated separately.

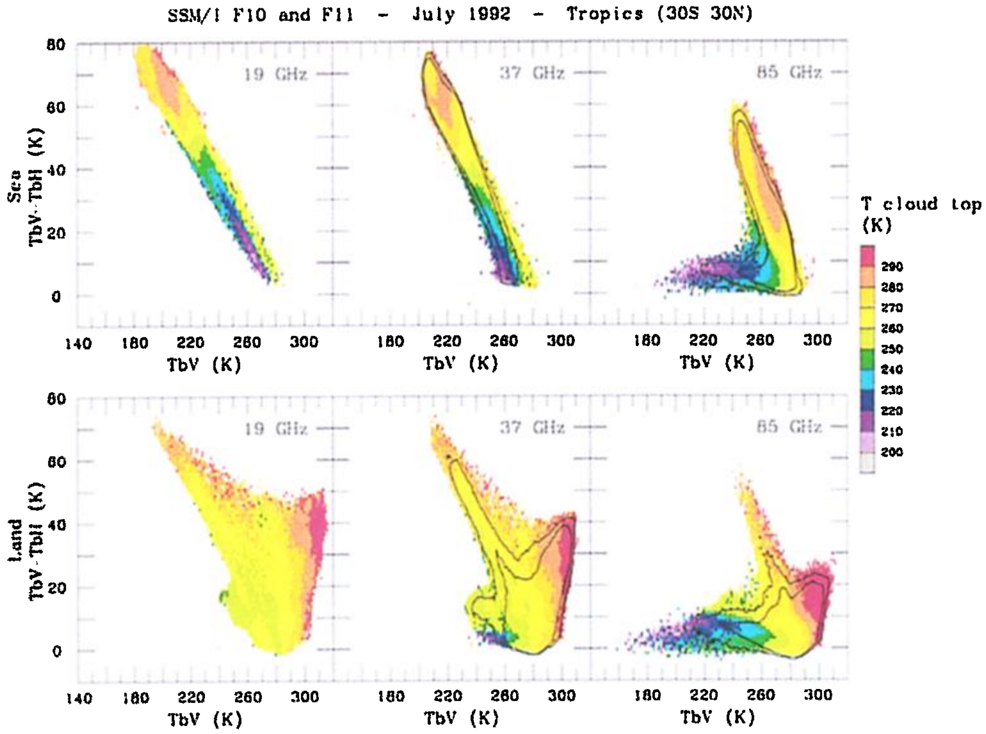

Plate 1. Scatterplots of the SSM/I brightness temperatures in the vertical polarization (TbV) versus the brightness temperature polarization differences (TbV-TbH), at 19, 37, and 85 GHz in July 1992 over the tropics for cloudy pixels only. The (top) sea and (bottom) land cases are treated separately. For each 1×1 K box the color indicates the mean cloud top temperature. Contours limit regions where the pixel population in the 1×1 K boxes is larger than 0.01% and 0.002% of the total population for a month.

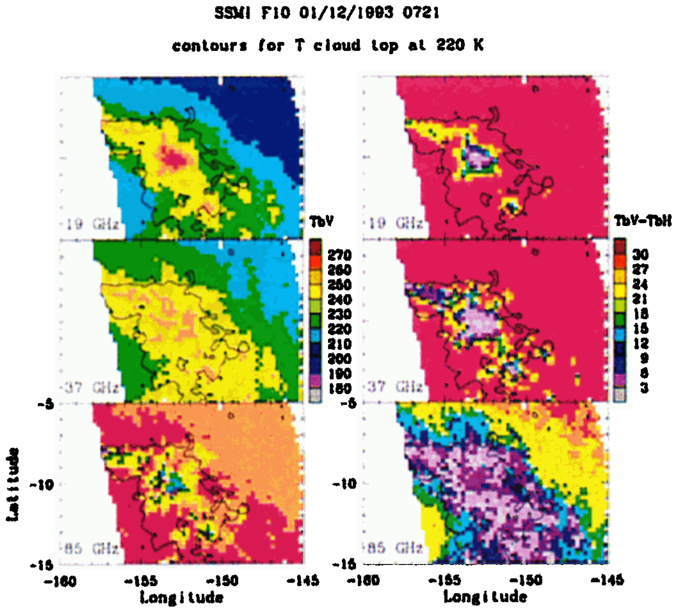

Plate 2. A cloud system over the Pacific ocean on January 12, 1993, at 0721 UT as seen from the F10 satellite by SSM/I at 19, 37, and 85 GHz for vertical and horizontal polarizations. The ISCCP cloud top temperature contours at 220 K are also shown.

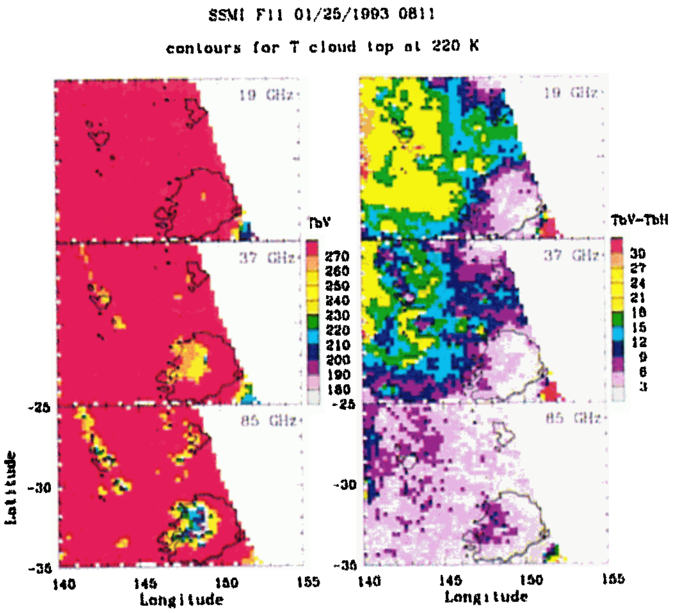

Plate 3. Same as Plate 2 but for a cloud system observed by the F11 satellite on January 25, 1993, at 0811 UT over southeast Australia.

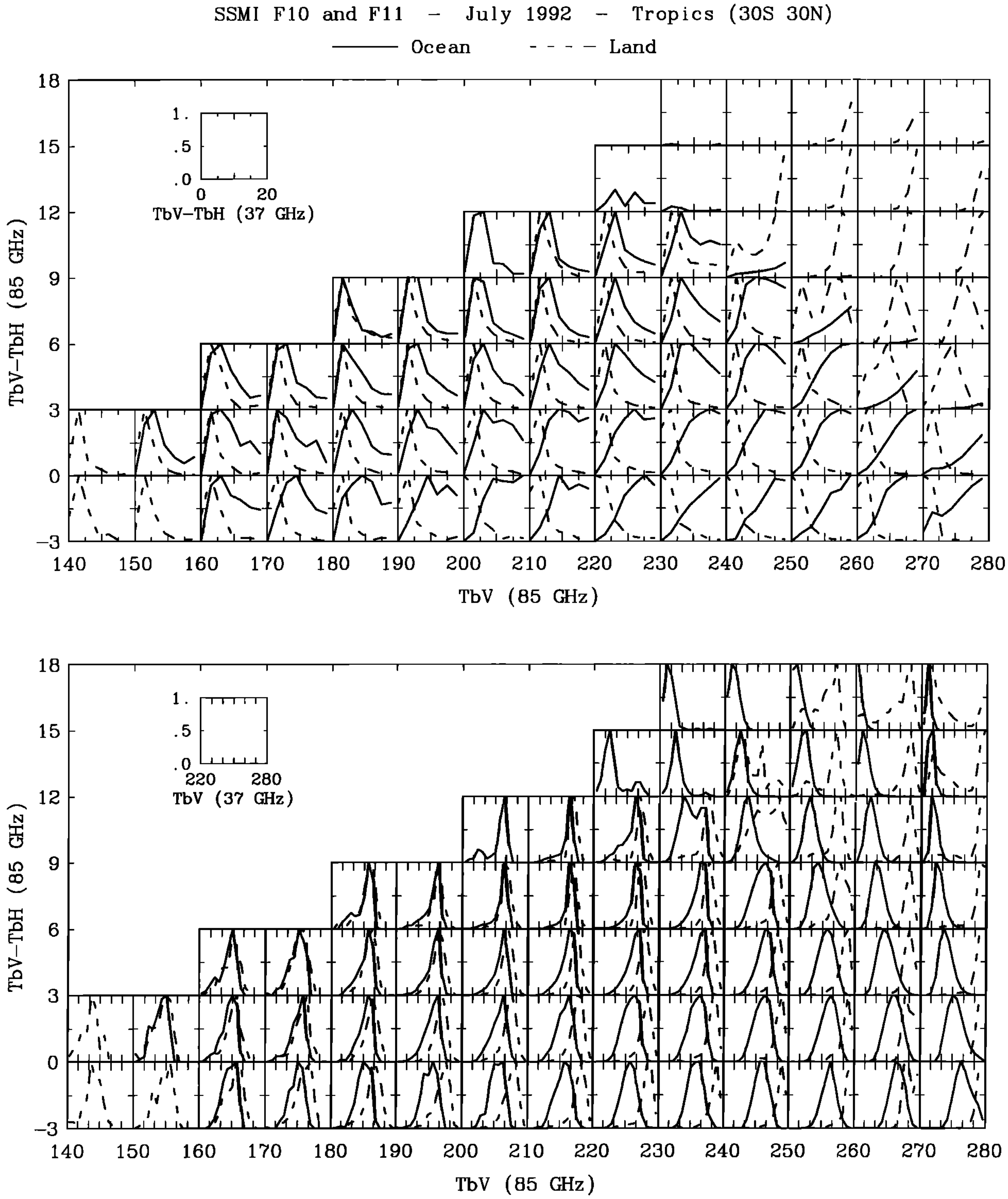

Figure 3. Same as Figure 2 for the TbV and TbV-TbH at 37 GHz.

polarization differences. The numbers in each box indicate the ratio of population density over land versus population density over ocean. The number of strong scattering cases (TbV(85)≤ 150 K) is more than twice as large over land than over ocean while the number of scattering cases at 85 GHz (190 K≤TbV(85)≤ 240 K) associated with large polarization difference (6 K ≤ TbV-TbH(85)≤ 12 K) is at least twice smaller over land than over ocean.

Is the polarization difference at 85 GHz generated within the cloud or is it related to some contribution from a polarized underlying surface? If the polarization difference emanates from the surface for these situations, the 37 GHz channel, which is less sensitive to absorption by cloud and rain particles, should also receive a significant contribution from the surface and be at least as polarized as the 85 GHz signature. The 37 GHz channel field of view, being also more than 4 times

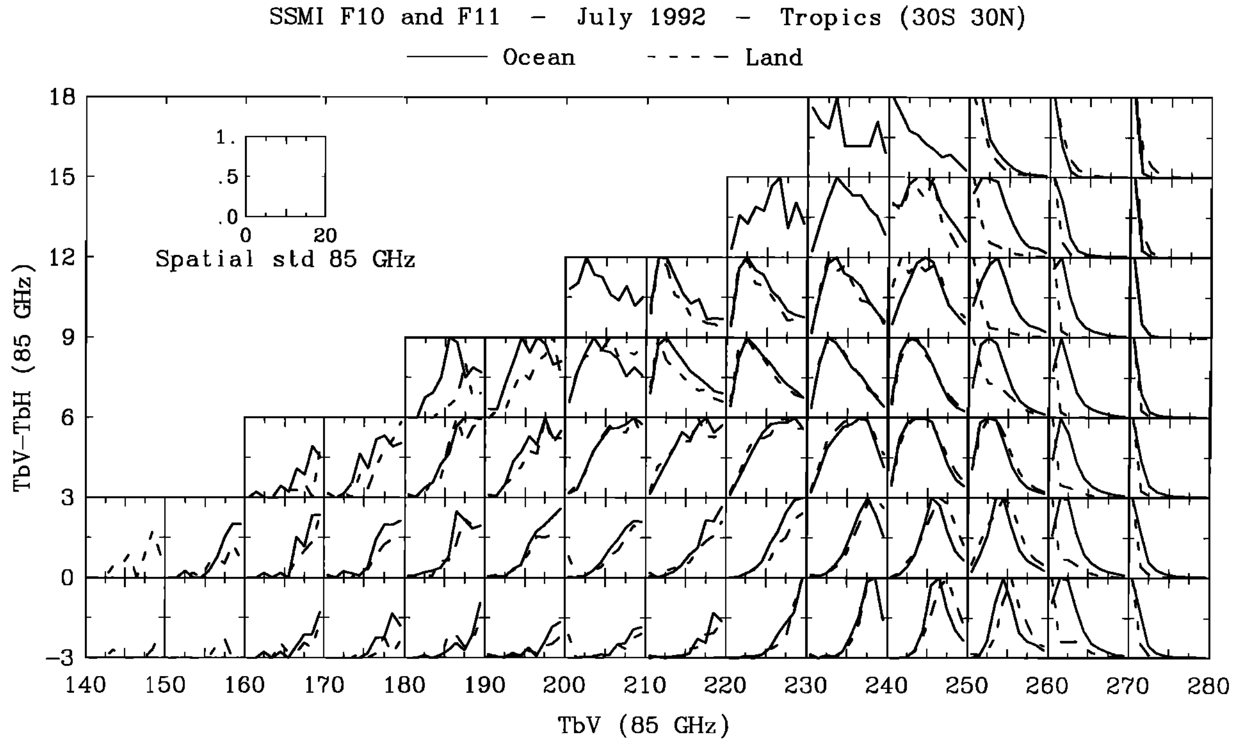

Figure 4. Same as Figure 2 for the standard deviation of the TbV at 85 GHz calculated for each $1/4^o \times 1/4^o$.

the size of the 85 GHz field of view, should also be more affected by spatial inhomogeneities. As in Figure 2, Figure 3 presents histograms of the TbV and TbV-TbH at 37 GHz for each 10 K TbV and 3 K (TbV-TbH) interval at 85 GHz. When the emission regime dominates (TbV(85)$>$ 250 K and TbV-TbH(85)$>$3 K), histograms of TbV(37) over ocean and land are different because of the different emission properties of the surfaces. However, in areas of significant scattering at 85 GHz (TbV(85)$<$ 230 K) the histograms of TbV(37) and TbV-TbH(37) over ocean and land are much closer, suggesting that only a small fraction of the radiation comes from the surface. This is even true when the polarization difference at 85 GHz is large (6 K $\leq$ TbV-TbH(85)$\leq$ 12 K); the TbV(37) histograms then show a narrow peak at ~260 K, which over the radiatively cold ocean indicate large emission/absorption. For TbV(85)$\leq$ 190 K, whatever the underlying surface, TbV(37) histograms peak around 250 K with broader left pointing tail, indicating that the 37 GHz radiation either comes from a very cold emitting cloud layer or has undergone scattering. The TbV-TbH histograms at 37 GHz show that in areas of dense clouds (based on ISCCP) the polarization difference does not reach zero at this frequency, even over land (histograms over land peak around 3 K for TbV(85)$\leq$ 240 K). The histograms at 19 GHz (not presented here) are always different over land and ocean, even when the optical thickness at 37 GHz is large enough to obscure the surface. Two factors contribute to this effect, the lower absorption by liquid particles at 19 GHz and the poorer spatial resolution at this frequency.

While the lower-frequency channels are sampled every 25 km, the 85 GHz channel is sampled every 12.5 km [*Hollinger et al.*, 1987]. The spatial standard deviation of the 85 GHz channel is calculated for each $1/4^o \times 1/4^o$, and the histograms of the standard deviation are presented in Figure 4, for each 10 K TbV and 3 K (TbV-TbH) at 85 GHz within the scattering regime. Scattering at 85 GHz (TbV(85)$\leq$240 K) with large polarization differences (6 K$\leq$ TbV-TbH(85)$\leq$ 12 K) occurs in regions of rather low spatial standard deviations at 85 GHz (mode values close to 5 K) as compared to areas where scattering is associated with low polarization differences. *Anagnostou and Kummerow* [1997] proposed using a similar "variability index" to classify stratiform and convective rainfall with the SSM/I 85 GHz channel, and this idea is further developed by *Hong et al.* [1999].

The ice optical thickness derived from the ISCCP data has also been examined in correlation with the scattering signatures at 85 GHz (not shown here). Although scattering signatures at 85 GHz are always associated with large ice optical depths ($\geq$10), there are no noticeable changes in the ice optical depth between moderate (TbV(85)~ 230 K) and strong (TbV(85)~ 180 K) scattering at 85 GHz. This is due to the relative insensitivity of visible scattering to the larger precipitation-sized particles.

Observations from July 1992 have been presented so far. The analysis of the two other months we studied (October 1992 and January 1993) show very similar results. Two particular situations, one over ocean and one over land, are examined closer to emphasize what has been revealed by the statistical analysis. Plate 2

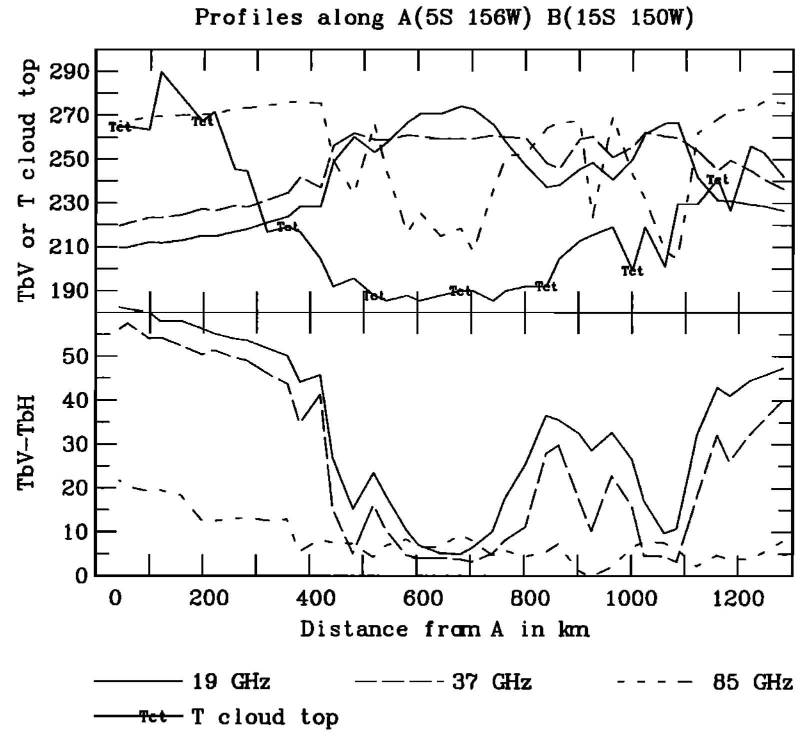

Figure 5. Cross section along point A(5°S 156°W) to point B(15°S 150°W).

shows a cloud system over the Pacific ocean on January, 12, 1993, at 0721 UT as seen from the F10 satellite by SSM/I at 19, 37, and 85 GHz for vertical and horizontal polarizations. The cloud top temperature contour at 220 K (also shown on Plate 2) is associated with TbV(19) and TbV(37) larger than 220 and 240 K, respectively, and also corresponds to a decrease of the TbV(85) below 250 K. Centered on 10°S and 153°W, a region of depressed TbV(85) indicates the presence of scattering at 85 GHz and is associated with TbV(19) larger than 270 K, implying heavy precipitation. The polarization difference in this area is higher at 85 GHz than at 19 and 37 GHz. As also shown on the profile in Figure 5, between 600 and 700 km and between 1000 and 1100 km from point A(5°S 156°W), TbV-TbH minima at 19 and 37 GHz coincide with polarization difference maxima at 85 GHz, proving that the polarized signatures at 85 GHz do not stem from the polarized surface but from the cloud structure itself.

A mesoscale convective system is observed with SSM/I on board the F11 satellite on January, 25, 1993 at 0811 UT over south east Australia (Plate 3). The surface emissivities in this area show large values with negligible polarization differences close to the coast and higher emissivity polarization differences farther inland (see the emissivity atlas described by *Prigent et al.* [1998, 2001]). The cloud structure centered at 32.5°S and 148°E is easily detectable not only at 85 GHz but also at 37 GHz, as TbV which is usually very warm over the land surface is depressed by the presence of cold emitters and scatterers. A profile through this cloud structure (Figure 6) shows a sharp decrease of the TbV(85) at 1000 km from A(25°S 140°E) that also corresponds to an increase in the polarization difference at the same frequency. The polarization difference at 85 GHz cannot be attributed to the surface which is weakly polarized. For 150 km the signatures are stable, and then TbV(85) decreases again over a small area along with the 37 and 19 GHz. The polarized scattering signals associated with TbV(85) around 220 K are located in the stratiform region of the system, while in the convective core, very low TbV are observed at 85 and 37 GHz and are associated with a decrease of the polarization difference at 85 GHz.

Our analysis of the scattering signature at 85 GHz suggests the following conclusions:

1. "Strong" and spatially variable scattering signatures at 85 GHz (TbV(85)$\leq$ 190 K) are associated with small polarization difference (mean TbV-TbH(85)$\leq$ 3 K) and are observed more frequently over land than over ocean. They coincide with low cloud top temperatures (Tc $\sim$ 200 K) that characterize deep convection. They are also associated with low TbV(37) ($\leq$ 250 K) implying emission by cold hydrometeors and scattering at 37 GHz. This suggests that these scattering signatures are concentrated in the convective cores of the cloud system where large vertical motions take place, especially over land. The proportion of ocean and land deep convective cases identified in this way in the SSM/I data is compatible with *Machado and Rossow*'s [1993] analysis of IR satellite measurements who also found higher occurrence of deep convection over land than over ocean.
2. "Moderate" and less spatially variable scattering signatures with TbV(85) between 220 and 250 K are asso-

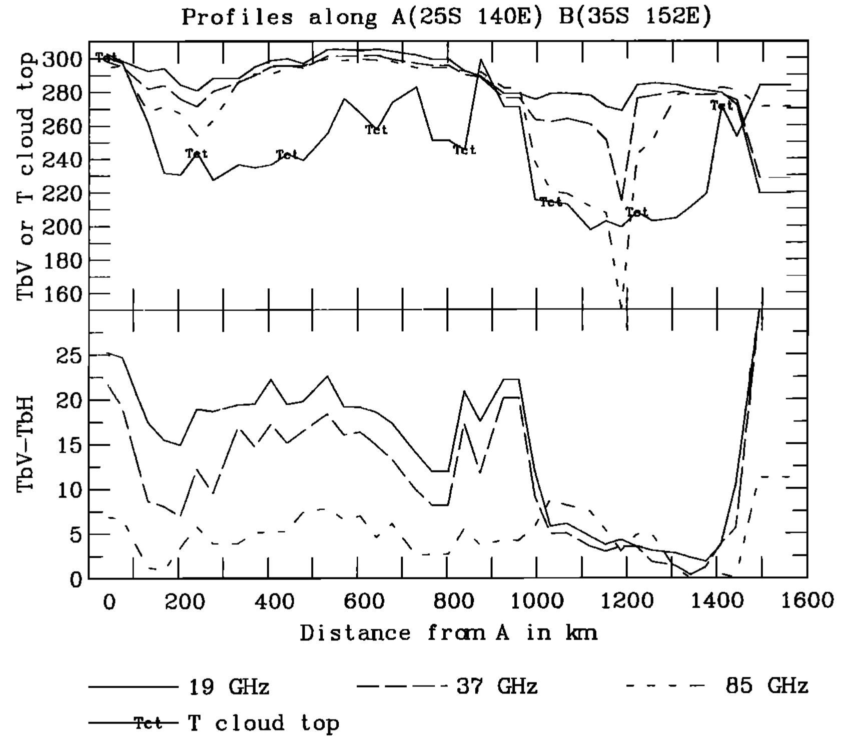

Figure 6. Same as Figure 5 but along point A(25°S 140°E) to point B(35°S 152°E).

ciated with large polarization differences TbV-TbH(85) that can reach ~12 K. These signatures are more frequent over ocean. For scattering situations with TbV(85)≤ 250 K, polarization differences larger than 6 K represent ~50% of the situations over ocean and ~40% over land. The polarization differences do not stem from the surface but are generated within clouds with top temperatures ~210 K, optical thicknesses above 10 in the VIS, high liquid water contents (small polarization difference at 37 GHz associated with TbV(37)~ 260 K). These characteristics are likely to be observed in the stratiform anvil of the convective cloud system as discussed by *Machado and Rossow* [1993] in their study of the average cloud properties in tropical convective systems from ISCCP data. *Machado and Rossow* [1993] also indicate that stratiform anvil clouds represent about 80% of the tropical convective systems and that one third of the anvil cloud may be associated with stratiform precipitation. These large proportions are consistent with the percentage of moderate scattering signatures at 85 GHz.

At 37 GHz the polarization difference rarely is negligible in regions of optically thick clouds. Given that similar signatures are observed over land and ocean, this polarization difference is unlikely to emanate from the surface alone.

Polarized microwave signatures in clouds could be associated with the "bright band" observed by radar. In precipitating stratiform clouds the radar detects a strong increase in reflectivity associated with the melting layer due essentially to change in particle permittivity and water coating effects at the onset of melting. This hypothesis will have to be investigated using collocated passive and active measurements from the Tropical Rainfall Measurement Mission (TRMM). Studies of the melting layer in the passive domain has recently motivated simulation studies [*Bauer et al.*, 1999], but no satellite investigation has been undertaken so far.

3. Development of a Radiative Transfer Model and Interpretation of the Observations

We have developed a radiative transfer model to explore the physical conditions that can explain the observed signatures. Our model combines into a single code T matrix routines to calculate the scattering by nonspherical particles, "doubling and adding" polarized radiative transfer through plane parallel layers composed of such particles, and a very up-to-date model of the microwave gas absorption in the atmosphere. It can be used to simulate radiances (including satellite viewing) in the longwave domain (up to 3 THz at present). The pure gas absorption of the atmosphere is taken from recent works by *Pardo et al.* [2001a, 2001b].

3.1. Description of the Model

The equation describing the transfer of radiation through an atmosphere that may contain scatterers is:

$$\mu\frac{dI(z,\mu,\varphi)}{dz} = K(z,\mu,\varphi)I(z,\mu,\varphi) - \int_{-1}^{1} d\mu' \int_{0}^{2\pi} d\varphi' Z(z,\mu,\varphi,\mu',\varphi')I(z,\mu',\varphi') - \sigma(z,\mu,\varphi)B[T(z)], \quad (1)$$

where I=(I,Q,U,V)^T is the Stokes vector column describing the radiation field, T denotes the transposed vector, K is the 4×4 extinction matrix, Z is the 4×4 phase matrix, σ is the 4×1 emission column vector, $B(T)$ is the blackbody radiance at temperature T, μ=cos(ϑ) (where ϑ is the nadir angle), φ is the azimuth angle, and z is the vertical coordinate in a plane-parallel atmosphere with z=0 at the surface. The frequency dependence of I, K, Z, σ, and B is implicit. The extinction and phase matrices and the emission vector are related according to

$$K_{i1}(z,\mu,\varphi) = \int_{-1}^{1} d\mu' \int_{0}^{2\pi} d\varphi' Z_{i1}(z,\mu,\varphi,\mu',\varphi') + \sigma_i(z,\mu,\varphi), i = 1,...4, \quad (2)$$

which is a consequence of the detailed energy balance [*Mishchenko et al.*, 1999].

The model is composed of three basic parts: The absorption by atmospheric gases, the scattering calculations for spherical and nonspherical hydrometeors, and the radiative transfer through an atmosphere with plane parallel layers in which different hydrometeors and/or atmospheric gases coexist.

The details about the absorption by atmospheric gases are given by *Pardo et al.* [2001a, 2001b]. Recent broadband Fourier transform spectroscopy measurements from the ground covering frequencies up to 1.6 THz [*Pardo et al.*, 2001a; *Matsushita et al.*, 1999; *Paine et al.*, 2000] have validated the longwave gas absorption model in the troposphere.

The far-field scattering by single nonspherical particles is computed using T matrix codes developed by *Mishchenko* [1991, 1993, 2000]. Two different codes have been used. First, the case of nonspherical randomly oriented axially symmetric particles is treated by means of very fast routines TMD (T matrix double precision routines) [*Mishchenko*, 1991, 1993]). The calculations are the fastest available for the considered case thanks to the use of analytical solutions. The second set of routines treats the case of totally oriented nonspherical particles (T matrix for single oriented particles [*Mishchenko*, 2000]). The use of these routines provides exactly the same result as the TMD routines if the phase matrices are integrated over all possible orientations, but the calculations typically take 10-100 times longer. However, these routines allow the simulation of scattering by an ensemble of partially oriented particles. Water droplets falling in the gravitational field or ice cloud particles aloft are examples of partially oriented nonspherical particles. For the integration over all possible orientations to be possible it is necessary to be in the independent scattering regime where each particle is in the far-field zone of the others. This implies that the average distance between particle centers is larger than 4 times their radius [*Mishchenko et al.*, 1995]. This requirement is usually satisfied by both cloud and precipitation particles. The scattered fields are then incoherent, and their Stokes parameters can simply be added.

To our knowledge, the radiative transfer codes that have been developped so far to simulate scattering by oriented aspherical particles can only handle perfectly oriented particles. In this study, we have introduced a degree of orientation of the spheroïd particles without breaking the azimuthal symmetry of the problem. This is possible by considering a random orientation of the projection of the particle axis in the azimuthal plane but limiting its vertical orientation to a given range with respect to the zenith direction. We have considered asphericities ([a=b]/c) larger than 1 (oblate particles) with axis tilting randomly from $\pi/2 - \alpha_0$ to $\pi/2$ with respect to the horizontal plane because that favors the more realistic case of the two larger particle axis being in or near the horizontal plane instead of in the zenith direction.

The assumptions described in the preceding paragraph allow the use of a simplified radiative transfer equation (that describes the behavior of the system from a macrophysical point of view) such as equation (1). In our simulations the plane parallel geometry is assumed with thermal emission as the only source of radiation. The hydrometeors can be either totally randomly oriented or at least azimuthally randomly oriented. In that case, the radiation field is azimuthally symmetric [*Evans and Stephens*, 1995] leading to vanishing Stokes parameters U and V; thus the dimension of the vectorial equation (1) is reduced to two:

$$\mu\frac{dI^0(z,\mu)}{dz} = K(z,\mu)I^0(z,\mu)$$

$$-2\pi\int_{-1}^{1} d\mu' Z^0(z,\mu,\mu')I^0(z,\mu') - \sigma(z,\mu)B[T(z)], \quad (3)$$

where the superscript zero denotes the zeroth azimuthal harmonic of the respective quantity, all matrices represent the upper left 2×2 blocks of the respective 4×4 matrices appearing in (1), and all column vectors have the dimension two and are composed of the upper two elements of the respective four-element column vectors.

The 2x2 radiative transfer equation is integrated using the quite standard method called doubling and adding, introduced in our model following *Evans and Stephens* [1995]. Three properties (the reflection matrix (R), the transmission matrix (T), and the source vectors (S)) are used in this method for the calculations. R and T have to be defined for each pair of "in" and "out" directions and S for each incident angle. A quadrature description is thus used for the zenith angle in the integration. All three properties are derived for a layer of infinitesimal thickness (Δz) from K, M, and σ by a discrete finite difference of (1).

3.2. Simulations and Interpretation of the Observations

The model allows the calculation of the Stokes parameters I and Q or brightness temperatures in two in-

Table 1. Results for Different Combinations of Plane -Parallel Hydrometeor Layers[a]

	Surface Hydrometeor layers	Characteristics of layer 3[a]	TbV(37) TbV-TbH(37)	TbV(85) TbV-TbH(85)
1	land 1		249.49 2.75	254.20 1.29
2	(ocean) 1		248.40 3.51	253.93 1.39
3	ocean 1+(2)		263.24 2.34	265.31 0.08
4	(land) 1+2		264.02 1.78	265.35 0.07
5	land 1+2+3	(0.2/400) (1.0/90)	262.19 2.05	246.60 0.40
6	land 1+2+3	(0.4)/400 1.0/90	261.41 2.04	228.68 0.48
7	land 1+2+3	0.4 /(200) 1.0/90	262.79 2.05	261.84 0.18
8	land 1+2+3	0.4 /(400) 1.4/90	261.48 2.04	230.15 0.48
9	land 1+2+3	0.4 /400 1.4/(20)	261.65 2.43	232.87 8.50
10	land 1+2+3+(4)	0.4 /400 1.4/20	261.91 2.35	239.30 7.30

[a] The four parameters given in column three are: Equivalent water path (kg/m^2)/ particle size (μm), and asphericity/ orientation parameter in degrees (the orientation of the particle axis is random in the azimuthal plane and limited to [$-\alpha_0 < \alpha < \alpha_0$] in the vertical direction, α is the angle with respect to the azimuthal plane). Input parameters that change in one row with respect to the previous are indicated by parentheses.

dependent linear polarizations in the phase plane (usually linear horizontal and linear vertical). Fresnel or Lambert like surfaces can also be introduced in the calculations, and a large number of parameters can be varied. Those parameters are frequency, observation nadir angle, surface type, atmospheric humidity and temperature profiles, hydrometeor vertical distribution, particle size and distribution, dielectric constant of the hydrometeors, particle asphericity, and degree of orientation of the hydrometeors (angle α_0 introduced in section 3.1).

In this study, we do not intend to fully explore the whole range of variations of all the hydrometeor parameters and their impact on all the SSM/I channels. Instead, we focus on the investigation of the parameters that are relevant to the explanation of the range of the observed polarized scattering signatures. Atmospheric profiles with plausible characteristics are selected as inputs to the radiative transfer model. The effects of realistic variations of the relevant hydrometeor parameters are analyzed.

A tropical standard atmosphere profile is used. It contains 45.5 kg/m^2 of water vapor and has a surface temperature of 299 K. The surface type changes in the simulations to illustrate how the surface is seen at the different SSM/I frequencies. The land surface emissivity is set at 0.95 for both polarizations, and the ocean is treated as a perfect Fresnel surface. The nadir angle of the simulated satellite observation is 50° which is close to the SSM/I scanning angle.

A number of simulations were performed to identify situations that compare well with the observed polarized scattering signals described earlier. Our analysis confirms the *Mugnai et al.* [1993] study of weighting functions in clouds. The 19 GHz channels are essentially sensitive to the rain layer, whereas the contribution of the liquid cloud is large for the 37 GHz channels, and the 85 GHz radiation does not sound below a thick ice layer when present.

Four plane-parallel hydrometeor layers are considered in our simulations, separately or in different combinations (1) a rain layer of 25 mm/h located between 0 and 5 km with a Marshall-Palmer drop size distribution; (2) a layer of liquid droplets between 5 and 6.5 km containing a liquid water path of 0.8 kg/m^2 with single-size spherical particles of 20 μm radius; (3) a layer of single-size ice particles between 6.5 and 8 km with character-

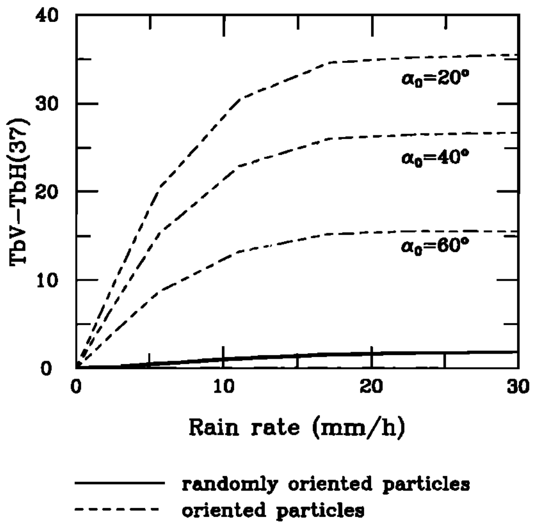

Figure 7. Sensitivity of the 37 GHz polarization difference to the orientation of the aspherical rain drops. The asphericity of the rain drop is 1.5.

istics that will vary for the different simulations; and (4) a layer of ice particles between 8 and 13 km with an equivalent water path of 0.1 kg/m^2 and single-size spherical particles of 30 μm radius.

Results for different combinations are presented in Table 1. For the rain and cloud liquid water layers the simulated brightness temperatures are similar over ocean and land at 37 and 85 GHz because the extinction is high enough to prevent the reception of radiation from the surface (compare rows 1-2 and 3-4). A polarization difference of ~2 K is calculated at 37 GHz over both land and ocean for simulations with rain and cloud liquid layers (rows 1 to 4). It is compatible with the polarization differences observed with SSM/I over optically thick clouds with mode values of ~3 K. No significant polarization difference is simulated at 85 GHz for these cases (rows 1 to 4). The polarization difference at 37 GHz is produced within the rain layer by scattering on spherical rain drops. Attenuation within the cloud is not large enough at 37 GHz to eliminate the polarization difference. With increasing rain rate, the polarization difference saturates around 2 K. With randomly oriented nonspherical particles, very similar results are obtained. However, for nonspherical oriented particles the polarization difference increases with rain rate and with the degree of orientation of the particles (Figure 7). Using different rain particle shapes and orientations, *Czekala et al.* [1998, 1999, 2001] have also simulated large polarization differences at 37 GHz. Nevertheless, given the spatial resolution of the SSM/I instrument at 37 GHz, the observed polarization difference in the scattering regime at 37 GHz never reaches large values. Although the particle size is not large enough to produce a significant scattering that can significantly depress the brightness temperature, the induced polarization difference is large enough to be detectable. At 19 GHz the rain and cloud liquid water layers do not totally block the surface radiation (not shown): Simulations over ocean and land are different, and over ocean the polarization difference generated at the surface is not completely masked by the hydrometeor layers.

Addition of an ice layer to the hydrometeor profile has a limited effect on the brightness temperatures at 19 GHz and 37 GHz, because of very low absorption and scattering by ice at these frequencies. At 37 GHz an ice water path of 0.4 kg/m^2 with 200 μm effective radius reduces the brightness temperatures by no more than 2 K in both polarizations. In contrast, the 85 GHz channels strongly react to the presence of the dense ice cloud, and its impact is highly dependent upon the ice quantity and the particle characteristics. For spherical ice particles the polarization difference is $\leq$ 0.5 K (rows 5 to 7); nonspherical randomly oriented particles do not generate high polarization difference either (row 8). Simulations are then performed to allow random orientations of the particle axis in the horizontal plane but restricting those orientations to a given range of α in the vertical plane. When the ice particles have an orientation restricted to $-\alpha_0 < \alpha < \alpha_0$ (with $\alpha_0 < 90^\circ$), the polarization difference increases as α_0 decreases reaching values observed with SSM/I at 85 GHz above cold clouds (row 9 in Table 1). Figure 8 shows the sensitivity of the 85 GHz brightness temperatures to the sphericity and orientation of the particles. For particle shapes close to spheres (asphericity of 1.1) the polarization difference does not increase much as the particles become more oriented, whereas it can reach large values for highly oriented particles. The effect of particle size in this ice layer is also presented in Figure 8 for an asphericity of 1.4 and different values of the parameter α_0. Polarization differences from 6 to 10 K appear for an effective radius of ~ 350-450 μm and $\alpha_0 \leq 40^\circ$ for the same ice water path of 0.4 kg/m^2.

The fourth cloud layer made of small ice particles only increases the microwave radiation at 85 GHz but does not affect much the polarization difference. This cloud layer is necessary to fit the mean 210 K cloud top temperature observed in the IR. Its ice water content of 0.1 kg/m ^{2} for effective particle radius of 30 μm corresponds to an optical thickness of 10 [*Rossow et al.*, 1996], similar to the ISCCP estimates in the areas of polarized scattering signatures at 85 GHz. From SAGE II and ISCCP estimates, *Liao et al.* [1995] have shown that in the tropics, 70% of the thick clouds have an extinction coefficient that gradually increases over a substantial vertical extent. The physical cloud top is usually located near the tropopause. The two ice layers schematically represent this phenomenon in our simulations.

These simulations support the SSM/I observations described in section 2 that correspond to scattered brightness temperatures of ~240 K and polarization differences $\geq$ 6 K at 85 GHz. Simulations at 37 GHz also fit the measurements for these same cases, with aver-

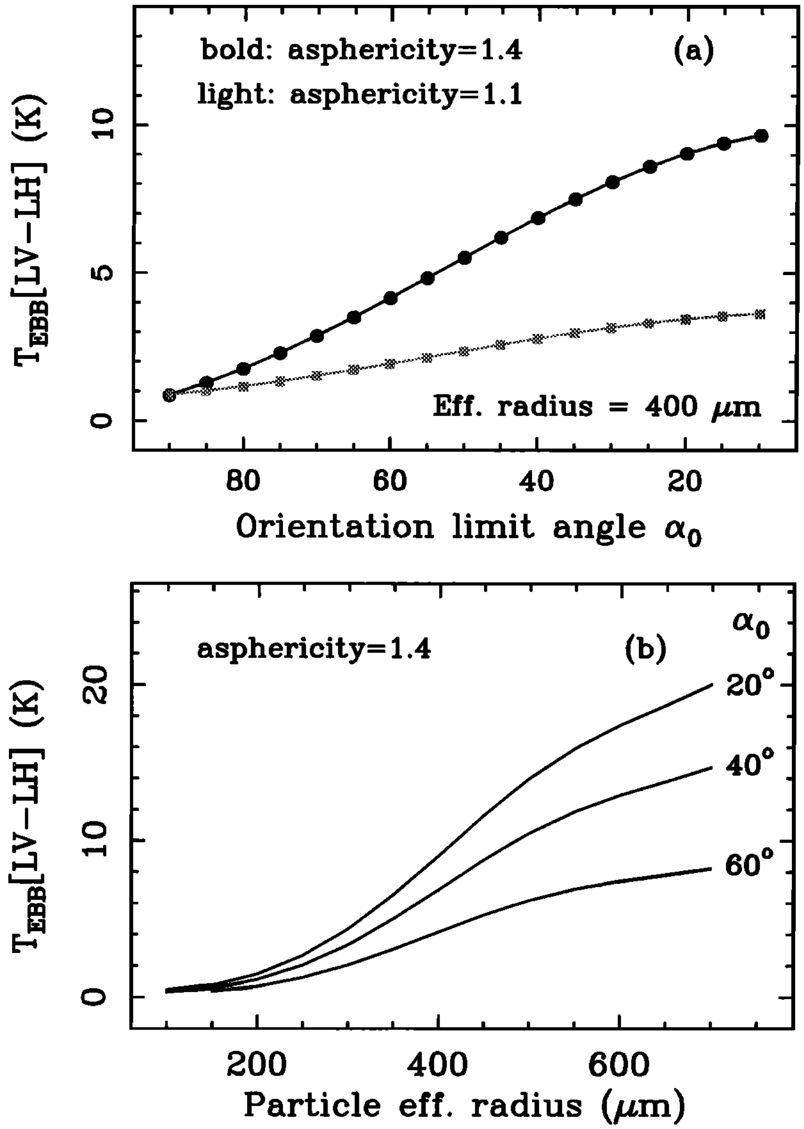

Figure 8. (a) Sensitivity of the 85 GHz polarization difference to the asphericity and orientation of the ice particles in the ice layer considered in the simulations (see text). (b) Effect of ice particle size on the 85 GHz polarization difference.

aged brightness temperatures ~260 K over both ocean and land and polarization differences ≥ 2 K. Other combinations of rain and liquid cloud layers could reproduce the microwave signatures present in the observations. However, whatever the liquid hydrometeor layers below, an ice layer with oriented, large, nonspherical particles is required to explain the large polarization signatures at 85 GHz.

4. Conclusion

SSM/I microwave observations of convective cloud systems in the tropics are studied for several months. A thorough analysis of the observed polarized scattering signatures is conducted with the help of cloud top temperatures and optical thicknesses extracted from visible and IR observations. Strong scattering signatures at 85 GHz with very low brightness temperatures (TbV(85)≤ 190 K) correspond to small polarization difference (TbV-TbH(85)≤ 3 K). They coincide with low cloud top temperatures, happen in areas of large spatial heterogeneity, and are observed more frequently over land than over ocean. This suggests that these scattering signatures are concentrated in the convective cores of the cloud system where large vertical motions take place, especially over land. Moderate scattering signatures (TbV(85)~230 K) are generally associated with mean polarization differences over ~6 K. They occur more often over ocean. In the scattering regime at 85 GHz (TbV(85)≤250 K) we showed that polarization differences ≥ 6 K occur ~50% of the time. The polarization difference does not stem from the surface but is generated within relatively homogeneous clouds having rather high liquid water content and cold cloud tops. These characteristics are observed in the stratiform anvils of convective cloud systems. In addition, the polarization difference observed at 37 GHz is never negligible over dense clouds whereas simple absorption/emission models for cloud and rain predict zero polarization difference over optically thick clouds.

To interpret these observations, a radiative transfer model that includes the scattering by spheroidal particles is developed, based on the T matrix approach and using the doubling and adding method. It does not only treat randomly or perfectly oriented particles but also simulates partially oriented spheroidal hydrometeors. Microwave brightness temperatures are calculated at SSM/I frequencies and are compared to the observations. A polarization difference of ~2 K at 37 GHz can be generated by emission/scattering in the rain layer even when using spherical particles; with oriented spheroidal particles, larger polarization differences can be simulated. The 85 GHz simulations are very sensitive to the ice phase of the cloud. Simulations with randomly oriented, large, spheroidal particles cannot replicate the observed polarization differences at 85 GHz, but oriented nonspherical particles can account for the observed signatures. Variations of the polarization difference with the degree of particle orientation are analyzed.

A large number of rain algorithms rely on the scattering signal at 85 GHz to detect and quantify rain rate. Recent developments include studies by *Mohr et al.* [1999] or *Liu and Curry* [1998]. These algorithms derive from radiative transfer calculations with simplified scattering schemes that assume spherical particles, i.e., negligible polarization differences generated in the hydrometeor layers. Several of them are based on indices like the polarization-corrected temperature defined by *Spencer et al.* [1989] (PCT=1.818TbV(85)-0.818TbH(85)). The magnitude of the polarized scattering signatures and the fact that it occurs almost 50% of the time in the scattering regime cannot be neglected when generating rain rate retrieval schemes based on the scattering properties of the hydrometeor layers. Although a full radiative transfer model may not be efficient in an operational implementation, the development of rain rate algorithms should take this feature into account to avoid systematically biased retrievals. Efforts are also directed toward retrieval of ice water amount in clouds from microwave observations based on radiative transfer simulations for up to submillimeter frequencies [e.g., *Evans et al.*, 1998; *Liu and Curry*, 1999; *Weng and Grody*, 2000], but great care must be exercised to fully represent the complexity of prevailing scattering signatures, such as described in this study.

Further analysis of cold cloud observations is planned using measurements from the Tropical Rainfall Measurement Mission (TRMM) satellite. Joint analysis of the passive and active measurements are projected, along with radiative transfer calculations for both active and passive modes. The TRMM microwave imager (TMI) has frequencies similar to SSM/I plus a 10.7 GHz channel, and it has enhanced spatial resolution compared to SSM/I (30×18 and 7×4 km at 19 and 85 GHz respectively). The radar at 13.8 GHz has a spatial resolution of 4 km. For mesoscale cloud model outputs, the radiative transfer code that has been developed will be used to generate simultaneously microwave brightness temperatures and backscattering coefficients that will be compared to the observations from the two instruments. Use of the two instruments, along with a synthetic radiative transfer code, will help better constrain the estimation of the hydrometeor characteristics and improve our understanding of the processes in the clouds. Special attention will be paid to the analysis of the passive measurements when radar "bright bands" are observed. A future paper will be devoted to a detailed description of the radiative transfer model itself and to an extensive exploration of the multidimensional space defined by all its parameters.

Acknowledgments. The authors are very grateful to Harald Czekala for his careful reading of the manuscript and his helpful comments. Valuable comments from G. Petty and two other anonymous reviewers were appreciated.

References

Adler, R. F., R. A. Mack, N. Prasad, H. Y. M. Yeh, and I. M. Hakkarinen, Aircraft microwave observations and simulations of deep convection from 18 to 183 GHz, part I, Observations, *J. Atmos. Oceanic Technol.*, *7*, 377-391, 1990.

Anagnostou, E. N,. and C. Kummerow, Stratiform and convective classification of rainfall using SSM/I 85 GHz brightness temperature observations, *J. Atmos. Oceanic Technol.*, *14*, 570-575, 1997.

Bauer, P., J. P. V. Poires Baptista, and M. De Iulis, The effect of the melting layer on the microwave emission of clouds over ocean, *J. Atmos. Sci.*, *56*, 852-867, 1999.

Colton, M. C., and G. A. Poe, Intersensor calibration of DMSP SSM/I's: F-8 to F-14, 1987-1997, *IEEE Trans. Geosci. Remote Sens.*, *37*, 418-439, 1999.

Czekala, H., and C. Simmer, Microwave radiative transfer with nonspherical precipitating hydrometeors, *J. Quant. Spectrosc. Radiat. Transfer*, *60*, 365-374, 1998.

Czekala, H., S. Havemann, K. Schmidt, T. Rother, and C. Simmer, Comparison of microwave radiative transfer calculations obtained with three different approximations of hydrometeor shape, *J. Quant. Spectrosc. Radiat. Transfer*, *63*, 545-558, 1999.

Czekala, H., S. Crewell, A. Hornbostel, A. Schroth, C. Simmer, and A. Thiele, Interpretation of polarization features in ground based microwave observations as caused by horizontally aligned oblate rain drops, *J. Atmos. Sci.*, in press, 2001.

Evans, K. F., and G. L. Stephens, Microwave radiative transfer through clouds composed of realistically shaped ice crystals, part II, Remote sensing of ice clouds, *J. Atmos. Sci.*, *52*, 2058-2072, 1995.

Evans, K. F., and J. Vivekanandan, Multiparameter radar and microwave radiative transfer modeling of non spherical atmospheric ice particles, *IEEE Trans. Geosci. Remote Sens.*, *28*, 423-437, 1990.

Evans, K. F., S. J. Walter, A. J. Heymsfield, and M. N. Deeter, Modeling of submillimeter passive remote sensing of cirrus clouds, *J. Appl. Meteorol.*, *37*, 184-205, 1998.

Ferraro, R. R., F. Weng, N. C. Grody, and A. Basist, An eight-year (1987-1994) time series of rainfall, clouds, water vapor, snow cover, and sea ice derived from SSM/I measurements, *Bull. Am. Meteorol. Soc.*, *77*, 891-905, 1996.

Fulton, R., and G. M. Heymsfield, Microphysical and radiative characteristics of convective clouds during COHMEX, *J. Appl. Meteorol.*, *30*, 98-116, 1991.

Greenwald, T. J., L. Stephens, T. H. Vonder Haar, and D. L. Jackson, A physical retrieval of cloud liquid water over the global oceans using the Special Sensor Microwave Imager (SSM/I) observations, *J. Geophys. Res.*, *98*, 18471-18488, 1993.

Grody, N. C., Classification of snow cover and precipitation using the Special Sensor Microwave Imager (SSM/I), *J. Geophys. Res.*, *96*, 7423-7435, 1991.

Haferman J. L., Microwave scattering by precipitation, in *Light Scattering by Nonspherical Particles*, edited by M.I. Mishchenko, J.W. Hovenier, and L.D. Travis, pp.481-524, Academic, San Diego, Calif., 1999.

Heymsfield, G. M,. and R. Fulton, Passive microwave and infrared structure of mesoscale convective systems, *Meteorol. Atmos. Phys.*, *54*, 123-139, 1994.

Hollinger, J. P., R. Lo, G. Poe, R. Savage, and J. Pierce, Special Sensor Microwave/Imager user's guide, Nav. Res. Lab., Washington, D. C., 1987.

Hollinger, J. P., J. L. Pierce, and G. A. Poe, SSM/I instrument evaluation, *IEEE Trans. Geosci. Remote Sens.*, *28*, 781-790, 1990.

Hong, Y., C. D. Kummerow, and W. S. Olson, Separation of convective and stratiform precipitation using microwave brightness temperature, *J. Appl. Meteorol.*, *38*, 1195,1213, 1999.

Kummerow, C., and L. Giglio, A passive microwave technique for estimating rainfall vertical structure information from space, *J. Appl. Meteorol.*, *33*, 3-17, 1994.

Liao, X., W. B. Rossow, and D. Rind, Comparison of SAGE II and ISCCP high-level clouds, 2, locating cloud tops, *J. Geophys. Res.*, *100*, 1137-1147, 1995.

Lin, B., and W. B. Rossow, Observations of cloud liquid water path over oceans: Optical and microwave remote sensing methods, *J. Geophys. Res.*, *99*, 20 907-20 927, 1994.

Liu, G., and J. A. Curry, Determination of characteristic features of cloud liquid water from satellite microwave measurements, *J. Geophys. Res.*, *98*, 5069-5092, 1993.

Liu, G., and J. A. Curry, An investigation of the relationship between emission and scattering signals in SSM/I data, *J. Atmos. Sci.*, *55*, 1628-1643, 1998.

Liu, G., and J. A. Curry, Tropical ice water amount and its relations to other atmospheric hydrological parameters as inferred from satellite data, *J. Appl. Meteorol.*, *38*, 1182-1194, 1999.

MacGaughey, G., E. J. Zipser, R. W. Spencer, and R. E. Hood, High-resolution passive microwave observations of convective systems over the tropical pacific ocean, *J. Appl. Meteorol.*, *35*, 1921-1947, 1996.

Machado, L. A. T., and W. B. Rossow, Structural characteristics and radiative properties of tropical cloud clusters, *Mont. Weather Rev.*, *121*, 3234-3260, 1993.

Matsushita S., H. Matsuo, J. R. Pardo, and S. Radford, FTS measurements of submillimeter-wave atmospheric opacity at Pampa la Bola II: Supra-terahertz windows and model fitting, *Publ. Astron. Soc. Jap.*, *51*, 603-610, 1999.

Mishchenko, M.I., Light scattering by randomly oriented axially symmetric particles, *J. Opt. Soc. Am.* A, 8, 871-882, 1991.

Mishchenko, M.I., Light scattering by size/shape distributions of randomly oriented axially symmetric particles of a size comparable to a wavelength, *Appl. Opt.*, *32*, 4652-4666, 1993.

Mishchenko, M.I., Calculation of the amplitude matrix for a nonspherical particle in a fixed orientation, *Appl. Opt.*, *39*, 1026-1031, 2000.

Mishchenko, M.I., D.W. Mackowski, and L.D. Travis, Scattering of light by bispheres with touching and separated components, *Appl. Opt.*, *34*, 4589-4599, 1995.

Mishchenko, M.I., J.W. Hovenier, and L.D. Travis, Concepts, terms, notation, in *Light Scattering by Nonspherical Particles*, edited by M.I. Mishchenko, J.W. Hovenier, and L.D. Travis, pp.3-27, Academic, San Diego, Calif., 1999.

Mohr, K. I., J. S. Famiglietti, and E. J. Zisper, The contribution to tropical rainfall with respect to convective system type, size, and intensity estimated from the 85 GHz ice-scattering signature, *J. Appl. Meteorol.*, *38*, 596-606, 1999.

Mugnai, A., E. A. Smith, and G. J. Tripoli, Foundation for statistical-physical precipitation retrieval from passive microwave satellite measurements. Part II: Emission-source and generalized weighting function properties of a time-dependent cloud-radiation model, *J. Appl. Meteorol.*, *32*, 17-39, 1993.

Paine, S., R. Blundell, D. C. Papa, J. W. Barrett, and S. J. E. Radford, A Fourier transform spectrometer for measurement of atmospheric transmission at submillimeter wavelengths, *Publ. Astron. Soc. Pac.*, *112*, 108-118, 2000.

Panegrossi, G., S. Dietrich, F. S. Marzano, A. Mugnai, E. A. Smith, X. Xiang, G. J. Tripoli, P. K. Wang, and J. P. V. P. Baptista, Use of cloud model microphysics for passive microwave-based precipitation retrieval: Significance of consistency between model and measurements manifolds, *J. Atmos. Sci.*, *55*, 1644-1673, 1998.

Pardo, J.R., E. Serabyn, and J. Cernicharo, Submillimeter atmospheric transmission measurements on Mauna Kea during extremely dry El Niño conditions: Implications for broadband opacity contributions, *J. Quant. Spectrosc. Radiat. Transfer*, *68*, 419-433, 2001a.

Pardo, J.R., J. Cernicharo, and E. Serabyn, Atmospheric transmission at microwaves (ATM): An updated model for mm/submm applications, *IEEE Trans. Antennas Propagat.*, in press, 2001b.

Petty, G. W., Physical and microwave radiative properties of precipitating clouds, part I, Principal component analysis of observed multichannel microwave radiances in tropical stratiform rainfall, *J. Appl. Meteorol.*, in press, 2001.

Phalippou, L., Variational retrieval of humidity profile,wind speed and cloud liquid water path with SSM/I: Potential for numerical weather prediction, *Q. J. R. Meteorol. Soc.*, *122*, 327-355, 1996.

Prabhakara, C., G. Dalu, G. L. Liberti, J. J. Nucciarone, and R. Suhasini, Rainfall estimation over ocean from SSMR and SSM/I microwave data, *J. Appl. Meteorol.*, *31*, 532-551, 1992.

Prigent, C., L. Phalippou, and S. English, Variational inversion of the SSM/I observations during the ASTEX campaign, *J. Appl. Meteorol.*, *36*, 493-508, 1997.

Prigent, C., W. B. Rossow, and E.Matthews, Global maps of microwave land surface emissivities: Potential for land surface characterization, *Radio Sci.*, *33*, 745-751, 1998.

Prigent, C., F. Aires, W. B. Rossow, and E. Matthews, Joint characterization of vegetation by satellite observations from visible to microwave wavelength: A sensitivity analysis, *J. Geophys. Res.*, *106*, 20,665-20,685, 2001.

Roberti, L., and C. Kummerow, Monte Carlo calculations of polarized microwave radiation emerging from cloud structure, *J. Geophys. Res.*, *104*, 2093-2104, 1999.

Rossow, W. B. and R. A. Schiffer, ISCCP cloud data products, *Bull. Am. Meteorol. Soc.*, *72*, 2-20, 1991.

Rossow, W.B., and R. A. Schiffer, Advances in understanding clouds from ISCCP, *Bull. Am. Meteorol. Soc.*, *80*, 2261-2287, 1999.

Rossow, W. B., A. W. Walker, D. E. Beuschel, and M. D. Roiter, International Satellite Cloud Climatology Project (ISCCP): Document on new cloud datasets, Natl. Aeronaut. and Space Admin., Goddard Inst. for Space Stud., New York, 1996.

Smith, E. A., A. Mugnai, H. J. Copper, G. J. Tripoli, and X. Xiang, Foundation for statistical-physical precipitation retrieval from passive microwave satellite measurements, part I, Brightness temperature properties of a time dependent cloud radiation model, *J. Appl. Meteorol.*, *31*, 506-531, 1992.

Spencer, R. W., B. B. Hinton, and W. S. Olson, Nimbus-7 37 GHz radiances correlated with radar rain rates over the Gulf of Mexico, *J. Clim. Appl. Meteorol.*, *22*, 2095-2099, 1983.

Spencer, R. W., H. M. Goodman, and R. E. Hood, Precipitation retrieval over land and ocean with the SSM/I: Identification and characteristics of the scattering signal, *J. Atmos. Oceanic Technol.*, *6*, 254-273, 1989.

Turk, J., and J. Vivekanandan, Effect of hydrometeor shape and orientation upon passive microwave brightness temperature measurements, in *Microwave Radiometry and Remote Sensing of the Environment*, edited by D. Solimini, pp.187-196, VSP, Zeist, Netherlands, 1995.

Turk, J., J. Vivekanandan, R. S. Marzano, R. E. Hood, R. W. Spencer, and F. J. Lafontaine, Active and passive microwave remote sensing of precipitating storm during CaPE, part I, Advanced microwave precipitation radiometer and polarimetric radar measurements and models, *Meteorol. Atmos. Phys.*, *54*, 3-27, 1994.

Weng, F., and N. Grody, Retrieval of ice cloud parameters using a microwave imaging radiometer, *J. Atmos. Sci.*, *57*, 1069-1081, 2000.

Wentz, F. J., A well calibrated ocean algorithm for Special Sensor Microwave Imager, *J. Geophys. Res.*, *102*, 8703-8718, 1997.

Wilheit, T. T., A. T. C. Chang, M. S. V. Rao, E. B. Rodgers, and J. S. Theon, A satellite technique for quantitatively mapping rainfall rates over the oceans, *J. Appl. Meteorol.*, *16*, 551-560, 1977.

Wu, R., and J. A. Weinman, Microwave radiances from precipitating clouds containing asphrical ice, combined phase, and liquid hydrometeors, *J. Geophys. Res.*, *89*, 7170-7178, 1984.

M. I. Michshenko and W. B. Rossow, NASA Goddard Institute for Space Studies, 2880 Broadway, New York, NY 10025, USA (mmishchenko@giss.nasa.gov; wrossow@giss.nasa.gov)

J. R. Pardo, CSCI, Instituto de la Estructura de la Materia, Departemento de Fisica Molecular, Serrano, 121, Madrid, 28006, Spain. (pardo@isis.iem.csic.es)

C.Prigent, CNRS, Département de Radioastronomie Millimétrique, Observatoire de Paris, 61, avenue de l'Observatoire, 75014 Paris, France. (catherine.prigent@obspm.fr)

(Received August 15, 2000; revised March 28, 2001; accepted June 1, 2001.)